Cement and Concrete Composites 146 (2024) 105374

Contents lists available at ScienceDirect

Cement and Concrete Composites

journal homepage: www.elsevier.com/locate/cemconcomp

Development and verification of an integrated hydration, geochemical and transport model for the hydrated cement paste exposed to an aggressive chemical environment

Siventhirarajah Krishnya [a,c], Kirushnapillai Kopitha [a], Yuya Yoda [b], Ryoma Kitagaki [a], Yogarajah Elakneswaran [a,*]

[a] Graduate School of Engineering, Hokkaido University, Sapporo-shi, Hokkaido 060-8628, Japan
[b] Shimizu Corporation, Shimizu Institute of Technology, Center for Construction Engineering, Japan
[c] Department of Civil Engineering, Faculty of Engineering, University of Jaffna, Ariviyal Nagar, Kilinochchi 44000, Sri Lanka

ARTICLE INFO

Keywords:
COMSOL-IPHREEQC
Carbonation
Chloride ion diffusion
Hydration products
Porosity
Cement paste

ABSTRACT

This study established a new transport model by using the COMSOL-IPHREEQC interface to simulate the changes in the morphology of hydrated cement paste due to the diffusion of carbon dioxide and chloride ion. A series of constitutive models such as the cement hydration model (to compute the dissolution rate of each clinker mineral), thermodynamic model (to perform the hydration reaction, reaction due to transport of ions, chemical and physical adsorption of chloride ion during the chloride ion ingression and dissolution rate of calcium-silica-hydrate (*C*–S–H) simultaneously with portlandite for the carbonation), porosity determination, and COMSOL Multiphysics (for the calculation of transport problems) were integrated using MATLAB language to determine the pore solution chemistry, hydrates assemblage, and porosity of the cement paste exposed to aggressive environments. During the diffusion of carbon dioxide gas, the decalcification of *C*–S–H was realistically considered by assuming that the Ca/Si ratio of *C*–S–H decreased from 1.67 (Jennite type *C*–S–H) to 0.67 (Tobermorite *C*–S–H), and then from 0.67 to 0 (silica gel). The proposed integrated platform was well verified with different sets of reported and raw experimental results and existing models, indicating a realistic predictability for chloride ion ingression and carbonation. The developed model discloses the effect of coupling the progression of hydration with reaction due to the transport of ions by using the free chloride ion profile and phase assemblages during the chloride ion ingression.

1. Introduction

With increasing interest in many fields of Civil Engineering, numerous research studies have focused on the durability of cementitious materials. Understanding and analysing multiple deterioration mechanisms affecting both new and existing concrete structures remain one of the most significant challenges, particularly while considering the long-term behaviour of the structure. This is, in turn, dictated by the capability of the concrete structures to a large extent to resist numerous deterioration processes such as transportation of ions-gas (mainly carbon dioxide) -moisture, alkali-aggregate reactions, and frost damage [1,2]. Worth to note that among the varying processes, chloride ingression and carbonation are the most severe degradation processes in reinforced concrete structures, specifically for those exposed to such environments as air-bone chlorides in marine regions and deicing salts in cold regions [3–5]. Under these environments, the processes occur concurrently as chloride ion penetrates from the seawater or deicing salts, and the carbon dioxide diffuses from the atmosphere, thus leading to an increase in the risk of reinforcement corrosion. The transport of these substances further involves chemical reactions between hydration products and pore solution, causing dissolution and precipitation in the hydrated matrix.

Chloride may enter the hydrated matrix in various ways, through the mixing water at the initial mixing stage or from the service environment. The external chloride ions can initiate corrosion when they reach the embedded reinforcement bar and accumulate to a threshold value. Subsequently, the formation of expansive corrosion products on the steel bar surface leads to destructive expansion and cracks. However, during the diffusion of chloride ions, a certain amount of ions tend to persist in

* Corresponding author.
E-mail address: elakneswaran@eng.hokudai.ac.jp (Y. Elakneswaran).

https://doi.org/10.1016/j.cemconcomp.2023.105374
Received 4 July 2023; Received in revised form 26 October 2023; Accepted 20 November 2023
Available online 25 November 2023

List of symbols and acronyms

$R^m_{t,1}$	Reaction rate of m clinker phase from the nucleation and growth mechanism [−]
$R^m_{t,2}$	Reaction rate of m clinker phase based on the diffusion mechanism [−]
$R^m_{t,3}$	Reaction rate of m clinker phase based on the formation of hydrated shells around the unreacted material [−]
α^m_t	Hydration degree of m clinker phase for the time of t [−]
$N^m_1, N^m_3, K^m_1, K^m_2, K^m_3$ and H^m	Equation constants related to the type of clinker [−]
Δt	Time interval [day]
$\frac{w}{c}$	Water to cement ratio [−]
RH	Relative humidity [−]
T	Temperature [K]
T_0	Reference temperature (293.15 K)
A	Blaine surface area of the cement [m^2/kg]
A_0	Reference surface area of cement (considered value 385 m^2/kg) [m^2/kg]
E^m_a	Apparent activation energy of clinker mineral [J/mol]
α_{C_3S}	Hydration degree of C_3S [−]
α_{C_2S}	Hydration degree of C_2S [−]
α_{C_3A}	Hydration degree of C_3A [−]
α_{C_4AF}	Hydration degree of C_4AF [−]
W_{C_2S}	Mass fraction of C_2S [%]
W_{C_3A}	Mass fraction of C_3A [%]
W_{C_4AF}	Mass fraction of C_4AF [%]
α_f	Total hydration degree of cement paste
W_{C_3S}	Mass fraction of C_3S [%]
$rate$	Dissolution rate of C–S–H [−]
R_1	Reaction rate constant [−]
γ_{CO2}	Material constant [−]
$W_{carb\ CSH}$	Weight of carbonated C–S–H [g]
$W_{tot\ CSH}$	Weight of total C–S–H [g]
M_{CSH}	Mol of C–S–H [mol]
M_{CO2}	Mol of CO_2 [mol]
M_r	The ratio of the mass of LD C–S–H to the total mass of C–S–H [−]
V_{CS}	Chemical shrinkage [g water]
Υ^m	Chemical shrinkage coefficient for clinker phase m [g water/g solid cement phase]
ζ^m	reacted weight of clinker phase m [g]
Φ_{Cap}	Volume fraction of capillary pore space [−]
V_i	Initial volume of the cement paste [cm^3]
V_{UC}	Unreacted clinker volume [cm^3]
V_{HP}	Volume of hydration products [cm^3]
$D_{e,l,i}$	Effective diffusion coefficient of i species ion in pore solution [m^2/s]
$D_{e,g,i}$	Effective diffusion coefficient of i species ion in gas phase [m^2/s]
$D_{0,l,i}$	Diffusion coefficient of i species ion in free water [m^2/s]
$D_{0,g,i}$	Diffusion coefficient of i species ion in gas phase [m^2/s]
Φ	Total active porosity (Φ_{Cap}+ gel porosity of LD C–S–H) [−]
δ	Tortuosity [−]
ϵ	Constrictivity [−]
S	Saturation degree [−]
$J_{l,i}$	Liquid phase ionic flux for species i in the pore solution [mol/m^2/s]
$J_{g,i}$	Gas phase ionic flux for species i in gas [mol/m^2/s]
J_i	Total ionic flux for species i [mol/m^2/s]
$C_{l,i}$	Concentration of i species in the liquid phases [mol/m^3]
$C_{g,i}$	Concentration of i species in the gas phases [mol/m^3]
Z_i	Electric charge number for species i [−]
φ	Electrical potential [V]
F	The Faraday constant [Coulombs/mol]
R	The universal gas constant [J/K/mol]
Q_i	sink term of species i (mol/m^3/s)
θ_l	Volume fraction of the liquid phase [−]
θ_g	Volume fraction of the gas phase [−]
k_i	Volatilisation factor [−]

the aqueous phase as mobile ions (interacting destructively with the passive layer of the steel bars), while the remaining ions are retained by the hydration products either by chemical binding or by physical adsorption [6–9]. Chemical binding refers to the reaction of chloride ion with AFm phases, which is shorthand for a family of aluminate–ferrite-mono substituent phases. Generally, the reaction of gypsum with aluminate (C_3A) produces ettringite, and further reaction of C_3A with ettringite forms monosulfate, the commonly available AFm phase in the OPC [10,11]. The sulfate ions in the monosulfate phase exchange with chloride ions in their presence, and the formed phase is referred to as Friedel's salt [7,12]. The physical binding of chloride ions is well known by the surface of the C–S–H, as it is the main hydration product in OPC and has a high specific surface area [13–15]. Therefore, the evaluation mechanism of diffusion of chloride ion in terms of free chloride ion, chemically bound chloride, and physically bound chloride is genuinely significant for developing models for service life prediction of reinforced concrete structures in the concern of reinforcement corrosion.

Carbonation of cement-based material is another complex process, altering the microstructural properties and performance of material subjected to atmospheric conditions. The diffusion of CO_2 gas through the pore network, followed by the reaction of CO_2 gas with the hydrated matrix, is commonly referred to as the carbonation process. Concrete structures must tolerate a certain level of carbonation reaction during their life owing to the existence of CO_2 gas in the atmosphere. However, this is a slow process, generally considered as a part of the prolonged degradation of concrete under typical atmospheric conditions. Most of the hydration products [mainly portlandite (CH) and calcium-silica-hydrate (C–S–H)] are consumed by the carbonation process and transformed to carbonate phases such as calcite, monocarboaluminate, hemicarboaluminate, amorphous silica gel, amorphous alumina gel and gypsum [16–18]. The reduction of internal alkalinity during the carbonation is the utmost significant problem in the concrete, as the dissolution of the thin oxide passive layer protecting the steel reinforcement is accelerated by low pH [19]. At the same time, the carbonation also poses positive effects in cement-basted materials. During the process, calcite deposition from the dissolution of portlandite and C–S–H occurs in pores, benefitting matrix densification and contributing to the development of mechanical properties and decreasing the transportation of hazardous ions [19–21]. However, when the porosity is sufficiently percolated for penetration of a significant amount of CO_2 gas, the process continues to consume Ca ions from C–S–H, resulting in the transformation to silica gel. This leads to the volumetric reduction or shrinkage and coarsening of the porosity [21]. During the combined ingression of chloride and carbonation, the physical and chemical chloride binding capacity in the hydrated matrix is decreased due to the carbonation reaction of portlandite and C–S–H, leading to more free chloride ions in the pore solution, which triggers rapid corrosion of the reinforcement [20].

Diffusion of ions and gases in the hydrated cement matrix is mainly influenced by its microstructure, defined by several factors such as the chemical composition of clinker, admixtures, supplementary

cementitious materials, water-to-cement ratio (W/C), curing method, curing temperature, hydration period and exposure conditions [22,23]. The microstructure/morphology of the hydrated cement paste can be mainly related to two spatial scales, namely nano-scale and micro-scale. The primary hydration product, known as *C*–S–H, exists in the nano-scale structure. The cement and concrete community is aware that the C–S–H forms in two different configurations: (i) low-density C–S–H (LD C–S–H) and (ii) high-density C–S–H (HD C–S–H) [24–26]. At the initial stage of the reaction, the *C*–S–H matrix nucleates on the outer surface of the clinker minerals, and with the progression of the hydration reaction, the formed *C*–S–H layer completely covers the cement particles. Formation of new *C*–S–H matrix is induced within the space confined by the previously formed *C*–S–H and unreacted clinker, as the ions continuously diffuse through the existing *C*–S–H matrix. The formed *C*–S–H at the initial stage as the outer product (hereinafter referred to as LD C–S–H) has a lower density than the *C*–S–H formed under the confinement as an inner product (hereinafter referred to as HD C–S–H). The pore spaces in the *C*–S–H matrix is defined as gel porosity, and the abovementioned two types of *C*–S–H have different size and volume of gel pores. The gel pores in the HD *C*–S–H have smaller pores than the LD *C*–S–H due to the limited space available for the formation of HD *C*–S–H. The morphology of the hardened cement paste comprises several mineral phases, including portlandite, monosulfate, ettringite, hydrogarnet and hydrotalcite at the micro-scale. The hydrated matrix also contains void spaces filled with air or water, called capillary porosity. The diffusion process in the hydrated cement matrix occurs through the capillary pores and partial gel pores of the *C*–S–H matrix.

Coupling the transportation processes and reactions between the transport of substances and solid phases in the matrix to capture the realistic changes of the porous matrix have gained a great deal of interest among researchers [5,6,15,19,27–30]. Elakneswaran et al. [28] developed a multi-ionic transport model using the PHREEQC for transportation and phase assemblage calculations by considering the phase equilibrium, surface complexation, and multi-component diffusion modules. Afterwards, the finite element software called COMSOL Multiphysics was combined with the geochemical program (PHREEQC or GEMS) to compute the transport and reaction calculation using computer languages such as Java and MATLAB [15,27]. Several researchers modelled the transportation of carbon dioxide gas to understand the solid phases and porosity changes in the hydrated matrix using the simple numerical and empirical modelling approach [19,29,30]. For another instance, the combined effect of carbon dioxide and chloride ion transportation on the phase assemblage, porosity and content of free chloride ion was analytically investigated by considering different aspects such as relative humidity, temperature and concentration of carbon dioxide gas [5,6]. These studies demonstrated that the transportation of ions and/or gases relies on several parameters such as the morphology of the porous matrix (pore solution chemistry, porosity and mineral phases), ionic diffusion coefficients, and exposure conditions. The phenomenological models are not sufficiently precise to predict the wide range of applications and are only limited to the range of fitted data. For modelling the transport properties of cement-based materials, incorporating the hydration process, chemical reaction, transportation process, and appropriate coupling among them is essential. However, due to the complexity of the coupling process, most of the previously developed models did not consider the hydration reaction simultaneously with the transportation process, and only considered the main hydration products without considering all the possible hydrates [5,6,15,19,29,30]. Therefore, addressing the limitations found in the previous models, a new framework is herein developed to predict the (i) chloride ion ingression and carbonation and (ii) phase assemblage due to the transportation process.

This proposed modelling platform is envisioned to be utilised for simulating the realistic behaviour of the hydrated matrix exposed to an aggressive environment, i.e., concurrent hydration and deterioration processes such as chloride ingression and carbonation. The platform developed in this study consists of several models, including the cement hydration model, thermodynamic model, porosity determination and transport calculation. The two types of *C*–S–H (low-density *C*–S–H and high-density *C*–S–H), other possible hydration products, and detailed calculation of chemical shrinkage are considered in the developed model for the realistic prediction of porosity, which is the significant factor determining mechanical and durability properties. The finite element package, COMSOL Multiphysics, is integrated herein to solve the transportation calculation effectively under the hydrated matrix's saturated and partially saturated conditions. The carbonation process is assumed as follows: CO_2 gas from the external environment diffuses through the gas phase of the hardened matrix, dissolves into the pore solution, transforms in the form of HCO_3^- and CO_3^{2-} and reacts with ions in the pore solution. In the case of chloride ingression, initially, chloride ions diffuse through the water-filled pore spaces and then react with ions and solid phases in the hydrated matrix. The proposed model is validated with raw experimental data and experimental results reported in the literature. The effect of coupled hydration reaction with reaction due to ion transport is also discussed.

2. Model description

This study details the proposed framework combining multiple constitutive models, including the cement hydration model, thermodynamic model, porosity determination and transport model developed in MATLAB language to predict the pore solution chemistry, hydration products and porosity of the hydrated cement paste exposed to an aggressive environment. The employed process and phenomena in the coupled model are schematically presented in Fig. 1. The elementary characteristics to determine the formation of hardened cement matrix during the hydration period, such as chemical and physical properties of cement, mixture recipe, and boundary conditions are the input parameters for the hydration model. Ionic concentration in the exposed environment, initiation of transport reaction relative to hydration time domain and duration of the transport reaction are the compulsory input data for the transport model as described in Fig. 1. The ensuing sections elaborate the adopted procedures of the developed model.

2.1. Hydration model

When water comes into contact with cement mixture, a series of simultaneous dissolution and precipitation processes are taken to form the hardened skeleton. This concept is generally referred to as the hydration of cementitious material, which is the fundamental process governing the development of intrinsic properties of the structure. The dissolution rate of clinker depends on several factors including W/C, curing temperature, relative humidity and surface area of particles [31,32]. However, each phase (C_3S, C_2S, C_3A and C_4AF) of the clinker dissolves with different dissolution rate. To simulate the hydration reaction degree of clinker with curing period, the empirical expressions associated with the abovementioned factors proposed by Parrot and Killoh [33] are adopted in this work. It must be noted that these empirical expressions were widely used and verified with experimental results in several previous studies [34–38]. In their approach, the reaction degree of each clinker phase is realistically considered by three main controlling mechanisms: nucleation and growth of products (Eq (1)), diffusion of ions through the layers of previously formed products (Eq (2)) and formation of hydrates shell around the unreacted material (Eq (3)). Among these three-reaction rates ($R^m_{t,1}$, $R^m_{t,2}$, $R^m_{t,3}$), the minimum value is selected as the actual controlling rate for calculating the hydration degree (α^m_t) for the time of t by using Eq. (4).

Nucleation and growth rate ($R^m_{t,1}$)

$$R^m_{t,1} = \frac{K^m_1}{N^m_1}\left(1-\alpha^m_t\right)\left(-\ln\left(1-\alpha^m_t\right)\right)^{\left(1-N^m_1\right)} \quad (1)$$

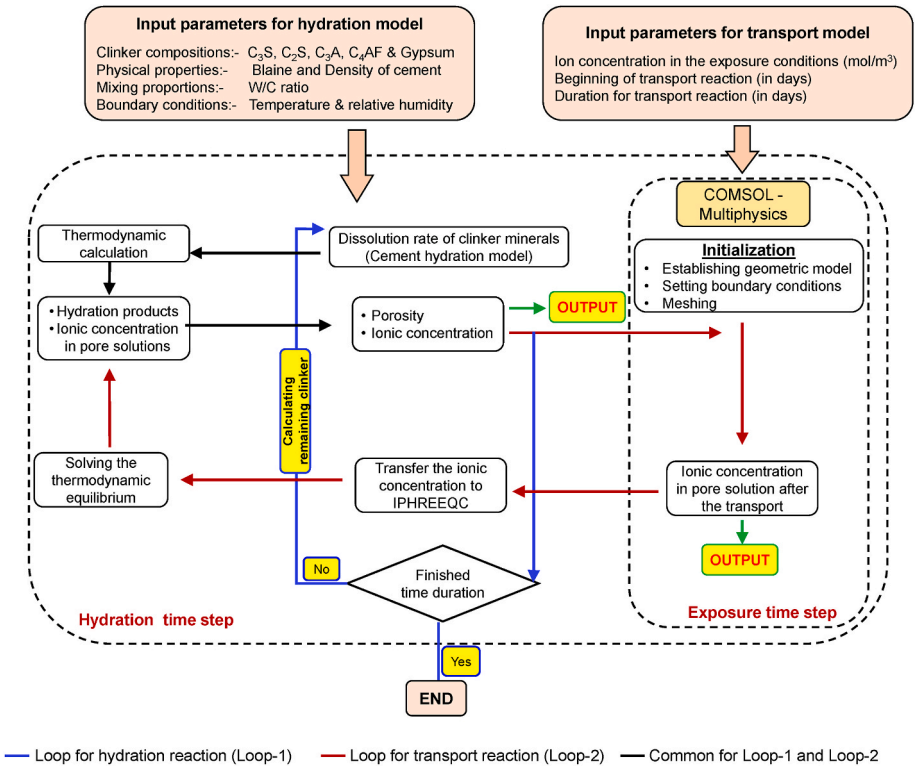

Fig. 1. Schematic diagram of the proposed coupled model.

Diffusion rate ($R^m_{t,2}$)

$$R^m_{t,2} = \frac{K^m_2\left(1-\alpha^m_t\right)^{\left(\frac{2}{3}\right)}}{1-\left(1-\alpha^m_t\right)^{\left(\frac{1}{3}\right)}} \tag{2}$$

Hydrates shell formation ($R^m_{t,3}$)

$$R^m_{t,3} = K^m_3\left(1-\alpha^m_t\right)^{N^m_3} \tag{3}$$

The hydration degree of a clinker mineral (α^m_t)

$$\alpha^m_t = \alpha^m_{t-1} + \Delta t \cdot \min\left(R^m_{t,1}, R^m_{t,2}, R^m_{t,3}\right) \cdot \beta_{w/c} \cdot \lambda_{RH} \cdot \frac{A}{A_0} \cdot \exp\left(\frac{E^m_a}{R}\left(\frac{1}{T_0}-\frac{1}{T}\right)\right) \tag{4}$$

where,

$$\beta_{w/c} = \left(1+3.333\cdot\left(H^m\cdot\frac{w}{c}-\alpha^m_{t-1}\right)\right)^4 for \alpha^m_{t-1} > H^m\cdot\frac{w}{c} \tag{5}$$

$$\beta_{w/c} = 1 \; for \alpha^m_{t-1} \le H^m\cdot\frac{w}{c} \tag{6}$$

$$\lambda_{RH} = \left(\frac{RH-0.55}{0.45}\right)^4 \tag{7}$$

In the above equations, T denotes the actual curing temperature in K, T_0 refers to a reference temperature (293.15 K), Δt is the time interval, $\frac{w}{c}$ is water to cement ratio, RH is relative humidity, A is the Blaine surface area of the cement (m^2/kg), A_0 is the reference surface area of cement (385 m^2/kg), E^m_a is the apparent activation energy of clinker mineral, K_1, N_1, K_2, K_3, N_3, and H are equation constants related to the type of clinker mineral. The constant values used for OPC are presented in Table 1.

Based on the estimated hydration degree of individual clinker phases (α_{C_3S}, α_{C_2S}, α_{C_3A} and α_{C_4AF}), the total degree of hydration of cement paste (α_f) for a specific time step is calculated as described in Eq. (8).

Table 1
The constants used to calculate the hydration degree of OPC clinker phases [34,35].

	C_3S	C_2S	C_3A	C_4AF
K_1	1.5	0.5	1	0.37
N_1	0.7	1	0.85	0.7
K_2	0.05	0.006	0.04	0.015
K_3	1.1	0.2	1	0.4
N_3	3.3	5	3.2	3.7
H	1.8	1.35	1.6	1.45
E_a (J/mol)	41,570	20,785	54,040	34,087

$$\alpha_f = \frac{\alpha_{C_3S}.W_{C_3S} + \alpha_{C_2S}.W_{C_2S} + \alpha_{C_3A}.W_{C_3A} + \alpha_{C_4AF}.W_{C_4AF}}{W_{C_3S} + W_{C_2S} + W_{C_3A} + W_{C_4AF}} \tag{8}$$

where, W_{C_3S}, W_{C_2S}, W_{C_3A} and W_{C_4AF} are mass fractions of each clinker phase.

When cement is mixed with water, K, Na, and S ions are released into the pore solution from the dissolution of the soluble alkali sulphates, and the less soluble minerals (for instance, gypsum and calcite) partially dissolve until equilibrium with the pore solutions is reached. It is assumed here that the gradually dissolved clinker phases continuously release Ca, Si, Al, Fe and hydroxide ions with respect to the reaction degree of individual phases, whereas minor components in the hydrated cement paste (such as Na_2O, K_2O and MgO let Na, K, Mg and O ions) get into the pore solution as the function of the total degree of hydration (α_f) for a specific time.

2.2. Thermodynamic model

In this study, thermodynamic calculations are executed using free geochemical software called PHREEQC, developed in C/C+ + by Parkhurst and Appelo, and which has been widely used for academic and industrial applications [15,39–41]. The default PHREEQC database,

along with cemdata18, is linked with the PHREEQC package as it requires a reliable thermodynamic database to perform the geochemical reaction for numerically predicting the interactions among water, gases, minerals, solid solutions, ion exchangers and surface complexation [39,42]. Phase equilibrium module, reaction module, surface complexation module and kinetic model for dissolution of *C*–S–H (for carbonation reaction only) are mainly entailed in the proposed model. The computed dissolved clinker phases from the cement hydration model (please refer to Section 2.1) are inputted in the reaction module for every hydration time step. The phase-equilibrium calculations are performed to define the stable hydration products that reversibly react with the pore solution to attain equilibrium, solving the law of mass action equation [43]. Portlandite, *C*–S–H, ettringite, gypsum, monosulfate, calcite, monocarbonate, hemicarbonate, hydrotalcite, stralingite, brucite, Fe–Al-silicieous hydrogarnet, Fe-silicieous hydrogarnet, Friedel's salt, amorphous silica and amorphous alumina gel are considered as equilibrium phases in the developed framework.

The physical binding of ions from the pore solution onto the surface of *C*–S–H has been investigated by several researchers [15,28,44,45]. Therefore, in the integrated model, the surface complexation module in PHREEQC is used to determine the ions' adsorption by the *C*–S–H surface by implementing the law of mass action relationships, charge potential relations for the surface and mole balance equations for surface sites. Based on the previous studies, it is assumed that the silanol site of *C*–S–H ($\equiv SiOH$) only reacts with ions in the pore solution, and the reaction with both calcium ($-CaOH$) and silandiol $= Si(OH)_2$ sites are ignored in this work [15,28,44]. The *C*–S–H produced from the hydration reaction of OPC is generally considered as Jennite type *C*–S–H with Ca/Si of 1.67. Thus, the specific surface area of jennite *C*–S–H used herein for the surface complexation calculation is 200 m^2/g [46], and the *C*–S–H site density is calculated based on the structural model proposed by Viallis-Terrisse et al. [47]. The adopted site reactions of *C*–S–H and the equilibrium constants are shown in Table 2.

From the thermodynamic perspective, all portlandite should be carbonated before the carbonation of *C*–S–H [48,49]. However, the experimental results for the carbonation of cementitious materials reveal that portlandite and *C*–S–H are carbonated simultaneously [50,51]. Therefore, a kinetic model for the dissolution rate of *C*–S–H (*rate*) is incorporated herein to simulate the actual condition and detailed in Eq. (9) [52]. This relationship is developed based on two assumptions: (i) the dissolution rate is proportional to the amount of *C*–S–H and CO_2 gas, and (ii) carbonate products from *C*–S–H dissolution are inversely proportional to the dissolution rate.

$$rate = R_1.\exp(\gamma_{CO2}.R_W).M_{CSH}.M_{CO2} \tag{9}$$

where,

$$R_W = \frac{W_{carb\ CSH}}{W_{tot\ CSH}} \tag{10}$$

$W_{carb\ CSH}$, $W_{tot\ CSH}$, M_{CSH}, and M_{CO2} are weight of carbonated *C*–S–H, weight of initial *C*–S–H, mol of *C*–S–H and mol of CO_2 respectively. R_1 and γ_{CO2} are reaction rate and material constant, and these values are defined by validation with experimental results.

Table 2
C–S–H surface site reactions and equilibrium constants.

Site reactions	$LogK_p$
$\equiv SiOH + OH^- \leftrightarrow \equiv SiO^- + H_2O$	−12.7
$\equiv SiOH + Ca^{+2} \leftrightarrow \equiv SiOCa^+ + H^+$	−9.4
$\equiv SiOH + Ca^{+2} + Cl^- \leftrightarrow \equiv SiOCaCl + H^+$	−8.9
$\equiv SiOH + Na^+ \leftrightarrow \equiv SiONa + H^+$	−13.64
$\equiv SiOH + K^+ \leftrightarrow \equiv SiOK + H^+$	−13.64

2.3. Porosity determination

A detailed porosity calculation is performed with the hydration period by considering all the possible hydration products and chemical shrinkage since porosity is one of the significant transportation factors. As mentioned earlier, the main hydration product, *C*–S–H, exists in two different characteristics (LD *C*–S–H and HD *C*–S–H) due to the available space for the hydration reaction. The formation of two types of *C*–S–H is incorporated in the proposed model based on the relationship detailed in Eq. (11) by distinguishing the total predicted weight of *C*–S–H from the thermodynamic calculation [10]. The average densities of LD and HD *C*–S–H are taken as 1700 kg/m^3 and 2000 kg/m^3, respectively [26].

$$M_r = 3.017.\frac{w}{c}.\alpha_f - 1.347.\alpha_f + 0.538 \tag{11}$$

where M_r, $\frac{w}{c}$ and α are ratio of the mass of LD *C*–S–H to the total mass of *C*–S–H, water-to-cement ratio and hydration degree, respectively. The hydrated cement's total amount of gel porosity depends on the *C*–S–H matrix's volume. Thus, reliable gel porosity values for HD *C*–S–H and LD *C*–S–H obtained from the literature are 26 % and 36 %, respectively [26].

The chemical shrinkage, defined as the reduction of the total volume of the hydrated matrix due to the molar volume difference between the cement clinker and the hydration products (i.e., initial volume of the mixture – volume of the hydrated matrix including water after the hydration reaction), is considered in the integrated framework by multiplying reacted clinker phases with the shrinkage coefficient of cement phases (refer Eq. (12)).

$$V_{CS} = \Upsilon^m \times \zeta^m \tag{12}$$

where, V_{CS}, Υ^m, and ζ^m are volume of chemical shrinkage (g water), chemical shrinkage coefficient for clinker phase *m* (can be obtained from Table 3) and reacted weight of clinker phase *m*.

The volume of two types of *C*–S–H is computed using their relevant densities, and other hydrates' volume is calculated based on their molar volume. The volume gap between the initial matrix and final matrix of hydrates, unreacted clinker and chemical shrinkage is considered as capillary porosity of the system, as given in Eq. (13).

$$\Phi_{Cap} = \frac{V_i - (V_{UC} + V_{HP} + V_{CS})}{V_i} \tag{13}$$

where, Φ_{Cap} is the volume fraction of capillary pore space, V_{CS} is chemical shrinkage, V_i is the initial volume of the matrix, V_{UC} is the unreacted clinker volume, and V_{HP} is the volume of hydration products.

2.4. Transport model

The COMSOL Multiphysics is used herein to solve the transport calculation of ions and gas between the porous and exposure conditions. The calculated ionic concentration (C_i) from the thermodynamic model, porosity (Φ is the summation of capillary porosity and gel porosity of LD *C*–S–H) and effective diffusion coefficient ($D_{e,i}$) of the hydrated matrix

Table 3
Chemical shrinkage coefficients [53].

Cement phase	Coefficient (Υ^m)/(g water/g solid cement phase)
C_3S	0.0704
C_2S	0.0724
C_3A (Convert all C_3A to ettringite)	0.171
C_3A (Convert all C_3A to Monosulfoaluminate)	0.115
C_4AF (Convert all C_4AF to ettringite)	0.117
C_4AF (Convert all C_4AF to Monosulfoaluminate)	0.086

are the initial conditions for the transport calculation, and they are transferred to the COMSOL package via LiveLink for MATLAB offered in the COMSOL Multiphysics. The ion concentration profile of each ion in the pore solution and exposure solution is computed based on the defined boundary conditions and the time step. The critical expressions used in this research work to compute the transport problem are briefly described here. The effective diffusion coefficient of ions in pore solution ($D_{e,l,i}$) and gases in the gaseous phase of the porosity ($D_{e,g,i}$) can be determined as a function of porosity, pore network parameters such as tortuosity (δ), constrictivity (ϵ), and saturation degree (S) as described in Eq. (14) and Eq. (15) [2,19,54,55].

$$D_{e,l,i} = D_{0,l,i}.S.\epsilon.\Phi^{\delta} \tag{14}$$

$$D_{e,g,i} = D_{0,g,i}.(1-S)^{4.2}.\epsilon.\Phi^{\delta} \tag{15}$$

where, $D_{0,l,i}$ and $D_{0,g,i}$ are the diffusion coefficient of ions in free water (m^2/s) and the diffusion coefficient of the gas in air (m^2/s), respectively. The considered values for the calculations are tabulated in Table 4.

The Nernst-Plank equation generally describes the ionic flux in the pore solution's liquid phase ($J_{l,i}$), as detailed in Eq. (16).

$$J_{l,i} = -D_{e,l,i}.\nabla C_{l,i} - D_{e,l,i}C_{l,i}.\frac{Z_i F}{RT}.\nabla\varphi \tag{16}$$

The flux in the gas phase ($J_{g,i}$) is illustrated in Eq. (17)

$$J_{g,i} = -D_{e,g,i}.\nabla C_{g,i} \tag{17}$$

The total flux (J_i) ($mol/m^2/s$) in the porous media can be defined by Eq. (18)

$$J_i = J_{l,i} + J_{g,i} \tag{18}$$

Where C_l, C_g, Z, F, R, T and φ are the concentration of species in the liquid phases (mol/m^3), the concentration of species in the gas phase (mol/m^3), the electric charge number, the Faraday constant, the universal gas constant, the absolute temperature, and the electrical potential (V), respectively. During the ion diffusion process in liquid, the electrical current is zero, which therefore implies [15],

$$F\sum_i Z_i j_i = 0 \tag{19}$$

The governing equation used in COMSOL Multiphysics for variably saturated flow is described in equations from Eq. (20) to Eq. (24).

$$\frac{\partial(\theta_l C_{l,i})}{\partial t} + \frac{\partial(\theta_g C_{g,i})}{\partial t} + \nabla.J_i = Q_i \tag{20}$$

$$\theta_l = \Phi.S \tag{21}$$

$$\theta_g = \Phi(1-S) \tag{22}$$

$$C_{g,i} = k_i.C_i \tag{23}$$

$$\frac{\partial(\theta_g C_{g,i})}{\partial t} = \theta_g k_i.\frac{\partial(C_i)}{\partial t} + k_i C_i.\frac{\partial(\theta_g)}{\partial t} \tag{24}$$

Table 4
Diffusion Coefficient of ions in free water at 20 °C.

Ion	Diffusion coefficient x 10^{-9} (m^2/s)
Na^+	1.33
Cl^-	2.03
K^+	1.96
Ca^{+2}	0.793
Mg^{+2}	0.705
$SO4^{-2}$	1.07
OH^-	5.27
$CO_2(g)$[a]	16,000

[a] Diffusion coefficient of CO_2 gas in air.

C, Q, θ_l, θ_g and k are the total concentration (mol/m^3), the sink term ($mol/m^3/s$), the volume fraction of the liquid phase, the volume fraction of the gas phase and volatilisation factors correspondingly. The sink term is computed based on the dissolution and precipitation of phases during the thermodynamic equilibrium process using PHREEQC. The relationship between the relative humidity (RH) and the saturation degree (S) adopted in the developed model is given by the inversion of the desorption isotherm expression, as shown in Eq. (25) [30].

$$S = \mu RH^3 + \beta RH^2 + \omega RH + \tau \tag{25}$$

where, $\mu = 6.427$, $\beta = -15.46$, $\omega = 12.52$, $\tau = -2.52$.

In this study, the concentration profile of each ion/gas in the pore system was computed by combining Eq. (18) – Eq. (20).

2.5. Coupling procedure

This proposed model is developed in MATLAB language, and the required input parameters can be updated through an Excel file which is convenient for the user. The following steps are involved in the coupling process.

Step 1: **After** entering all the required parameters, the model starts the calculation by reading the input parameters from the specific Excel file and calculating the dissolution rate of each clinker phase and minor phase using the cement hydration model (refer to Section 2.1).
Step 2: The calculated dissolved minerals are transferred to the thermodynamic calculation to compute the amount of hydration products and ion concentration in the pore solution using PHREEQC (see Section 2.2).
Step 3: The capillary pore space of the hardened cement paste is computed based on the two types of *C*–S–H, other hydration products, unreacted clinker, and chemical shrinkage of the reacted clinker (Section 2.3). These three steps repeat until the beginning of the exposure condition, which can be defined by the user (see input parameters for transport calculation in Fig. 1).
Step 4: The calculated ions concentration in pore solution and porosity at the beginning of the exposure are used as the initial conditions for the transport calculation, and they are transferred to COMSOL Multiphysics via LiveLink™ for MATLAB® feature available in COMSOL. Based on the defined exposure condition and time step, the ionic concentration profiles are predicted using the relationship explained in Section 2.4 in COMSOL.
Step 5: Afterwards, the predicted ionic concentration with exposure distance is updated to the thermodynamic calculation to compute the amount of products and ion concentration using phase equilibrium, surface complexation and kinetic model for *C*–S–H, in order to maintain the thermodynamic equilibrium as the existing thermodynamic equilibrium between the pore solution and hydrates was broken due to the ion/gas transportation process.
Step 6: As the next step of this model, the outcomes of the thermodynamic calculation due to the transport of ions are used to react with dissolved clinker minerals for continuing the hydration reaction using the PHREEQC package.
Step 7: The predicted products are then converted to volume fractions for calculating the capillary porosity at that time step (similar to Step 3).
Step 8: The ion concentration after the hydration reaction (outcome of Step 6) is input to COMSOL Multiphysics as the initial parameters for the next time step (similar to Step 4).

These whole procedures are repeated until they reach the final time step, which the user defines. In this research work, Na^+, K+, Ca^{+2}, $H_2SiO_4^{-2}$, SO_4^{-2}, Cl^- and OH^- in pore solution and $CO_2(g)$ in the gas phase are mainly considered ions and gas in the porosity of the system

for participating in the transportation process. The mixture of clinker, gypsum and water filled capillary pores at the mixing time can be defined as cement paste, at the same time the mixture consists of unreacted clinker, hydration products, gel and capillary porosity, and chemical shrinkage can be defined as hydrated cement paste/hydrated matrix after the mixing stage.

Here, it should be noted that the formation of hydration products, capillary porosity and chemical shrinkage during the hydration reaction has already been validated with different sets of experimental results in our previous works [11,38].

3. Experimental programme for carbonation

OPC with the Blaine of 339 m^2/kg and density of 3.16 g/cm^3 was used to prepare cement paste samples with W/C of 0.3, 0.4 and 0.5, and the mineral composition of clinker obtained from X-ray diffraction measurements is shown in Table 5.

Initially, the cement mixture was mixed for approximately 3 min and then cast into the cylindrical moulds with 50 mm diameter and 100 mm height. After 24 h of casting, de-moulded samples were kept under sealed curing at 20 ± 2 °C for 28 days. Resin coating was then applied to all two faces except the top circle face of the cylinder. Samples were then kept for four months in the CO_2 chamber having a CO_2 concentration of 5 %, relative humidity of 60 % and 20 °C temperature, as shown in Fig. 2. After the carbonation, samples were cut into 2 mm thick discs from the exposed surface to identify the newly formed phases during the carbonation by using thermogravimetric (TG) analysis. Samples were ground with less than 75 μm particles for TG analysis, which was conducted using HITACHI TG/DTA 7220 under an N_2 flow environment with a 200 mL/min flow rate. The temperature was increased at a rate of 10 °C/min from 20 to 950 °C and maintained for 60 min, then decreased at a rate of 10 °C/min. Around 15 mg of the sample was weighed and used for measurements.

4. Results and discussion

4.1. Carbonation

4.1.1. Experimental results

The TG analysis performed on the hydrated samples with different W/C exposed in 5 % of CO_2 for four months and at different core depths (0–2 mm and 8–10 mm are shown as examples) are presented in Fig. 3. For all the samples (W/C 0.3–0.5 and depth 0–2 mm and 8–10 mm), three quite similar principal peaks are resolved between the temperature 20 °C to 860 °C with different weight loss percentages. Mass loss before 120 °C is detected in all samples due to dehydration of ettringite and loss of physically bound water inside the *C*–S–H [49,51,56]. Due to the carbonation of these phases, mainly *C*–S–H, the intensity of the endothermic peak between this range increases with core depth as the near-surface slice (0–2 mm) is more carbonated than the slice sawn at 8–10 mm depth. Owing to the progression of carbonation, similar to the *C*–S–H phases, the decomposition of portlandite observed at approximately between 400 and 450 °C (refer to the DTG curve) decreases with the slice cut from the core (8–10 mm) to the exposed surface (0–2 mm) [24,56]. The considerable weight loss between the temperature 450–750 °C can be seen in the DTG curve, which is mainly attributed to the release of CO_2 related to the decomposition of calcite [56,57]. In the TG analysis, various peaks related to the decomposition of different polymorphs of calcium carbonate are not significantly observed. Because the decomposition temperature of calcium carbonate is in the range between 450 °C - 750 °C. Due to the reaction between CO_2 gas and calcium-bearing phases in the hydrated matrix, calcite precipitation adjacent to the exposure surface is considerably higher than far from the surface, as shown in Fig. 3.

Table 5
Mineral composition of clinker.

Mineral composition	Wt. (%)
C_3S	60
C_2S	16
C_3A	07
C_4AF	12
Gypsum	04

4.1.2. Developed framework verification with the experimental results

In order to prove the accuracy of the developed integrated model, the simulated results for the hydrated cement paste with W/C of 0.3–0.5 are compared with raw experimental results (refer to Section 3 for the experimental conditions), as detailed in Fig. 4. It can be observed that the predicted results reasonably fit with the calcite and portlandite weight percentage measurement, as elaborated in Fig. 4. However, a slight deviation can be seen between experimental and numerical results in some grid points. During the experimental programme, samples were not maintained at 60 % relative humidity prior to the carbonation, as the cement paste specimens were immediately placed in the CO_2 chamber after 28 days of hydration. Consequently, the cement paste samples with different W/C contain different internal relative humidity due to the inconsistency of the available water for the hydration reaction. The internal relative humidity for the 0.3 W/C paste is considerably lower than the high W/C paste, as the loosely bound water in the low W/C paste is consumed for the hydration reaction due to the water deficiency for the reaction [11]. Thus, the internal relative humidity during the initial carbonation period may not be constant for all the samples. However, in the developed model, the relative humidity of all samples is assumed to be constant at 60 % during carbonation. This leads to a slight discrepancy between the experimental and numerical results.

The formation of calcite shows an increasing tendency with W/C and decreasing behaviour with the distance from the exposure surface, as depicted in Fig. 4. On the other hand, the portlandite content in the hydrated matrix decreases with W/C for the same grid point, and after approximately 11 mm from the exposed surface, it remains unchanged. This is because the calcium-bearing phases, mainly portlandite and *C*–S–H, dissolve due to the reduction in the pore solution's pH near the exposure surface as the penetrated CO_2 gas dissolves and forms as CO_3^{2-} and HCO_3^- and subsequently precipitates as carbonate products (such as calcite). The diffusion of CO_2 gas mainly depends on the porosity of the hydrated matrix, which increases with W/C owing to the more available space for the hydration reaction. Therefore, the diffusion of the gas increases with W/C. As a result, calcite formation and portlandite dissolution are high in the cement paste with a W/C of 0.5.

The numerical results for the changes in the phase assemblages are depicted in Fig. 5 for the variation of the volume fraction of the hydrated matrix with distance from the exposure due to the progression of carbonation. The cement paste sample of W/C 0.6 (with the clinker composition of C_3S 60 %, C_2S 16 %, C_3A 07 %, C_4AF 12 % and gypsum 4 %) after 28 days of hydration exposed to 10 % (v/v) of CO_2 for 5 years is considered for the simulation. The existence of portlandite, Jennite type *C*–S–H, ettringite, and monosulfate, along with minor quantities of siliceous hydrogarnet and hydrotalcite, are predicted as the hydrates of the non-carbonated matrix shown after approximately 70 mm from the exposure surface in Fig. 5. In the developed model, the carbonation of portlandite and *C*–S–H are simultaneously considered for the realistic prediction by using the kinetic model for the dissolution of *C*–S–H. It is worthwhile to note that the decalcification of *C*–S–H is herein assumed as follows: (i) Tobermorite *C*–S–H (Ca/Si of 0.67) is formed by the removal of Ca from the Jennite *C*–S–H (Ca/Si 1.67), and (ii) Tobermorite *C*–S–H is carbonated as silica gel due to the complete removal of Ca ion from the Tobemorite *C*–S–H. Therefore, during the initial stage of the carbonation process, secondary ettringite, hemicarbonate, monocarbonate and Tobermorite *C*–S–H form due to the reaction between

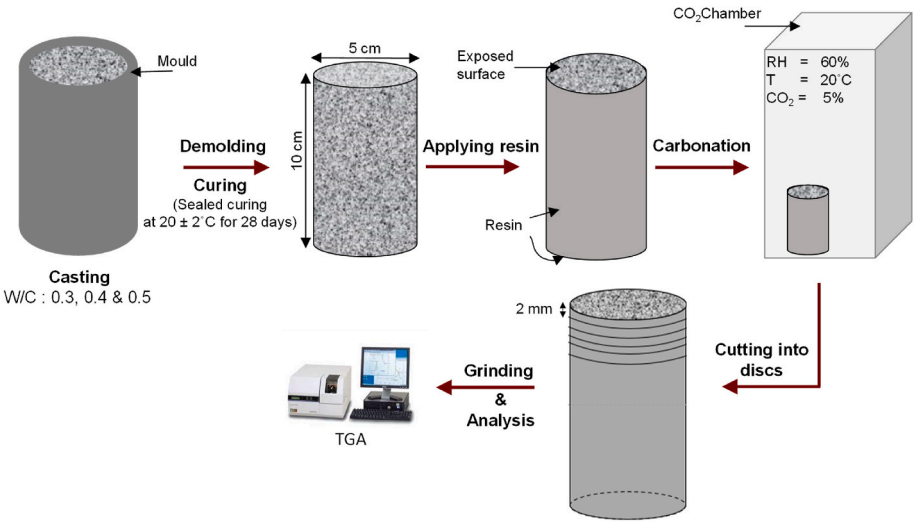

Fig. 2. Sample preparation and experimental condition for carbonation.

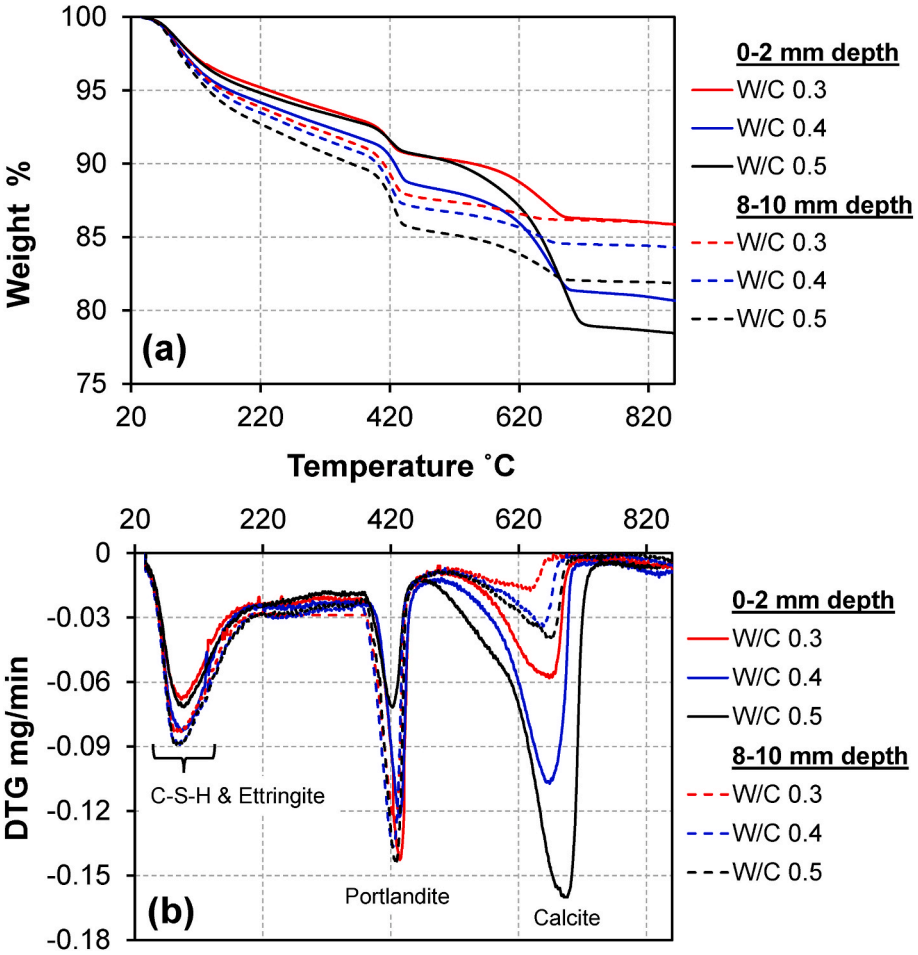

Fig. 3. TG analysis of the hydrated sample with W/C of 0.3–0.5 exposed in 5 % of CO_2 for four months: (a) weight % and (b) DTG.

CO_2, portlandite, monosulfate and Jennite *C*–S–H at the carbonation front (between 55 mm and 70 mm). As the carbonation continues, the remaining portlandite, monocarbonate and siliceous hydrogarnet (Fe, Al) are converted to strätlingite, Fe-siliceous hydrogarnet and calcite. Low Ca/Si *C*–S–H (Tobermorite) is further decalcified to silica gel after the depletion of monocarbonate and siliceous hydrogarnet (Fe, Al). Finally, ettringite is also destabilised to calcite, amorphous alumina and gypsum at low pH (approximately less than 10). Based on the predicted results, it can be seen that the total porosity (summation of capillary porosity and gel porosity) decreases from the non-carbonated matrix (right side) to the carbonation front (approximately 30 mm) and then increases towards the left side due to the complete carbonation of *C*–S–H

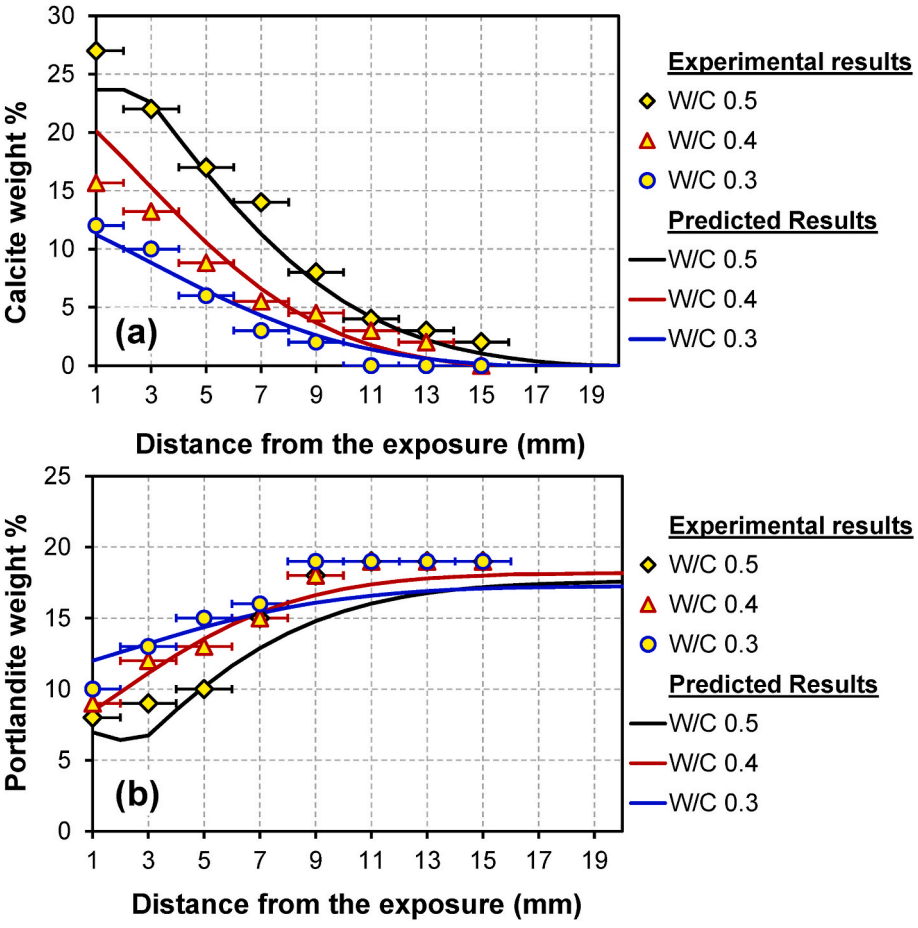

Fig. 4. (a) Calcite and (b) portlandite evolution profiles for W/C of 0.3, 0.4 and 0.5 samples after four months of accelerated carbonation.

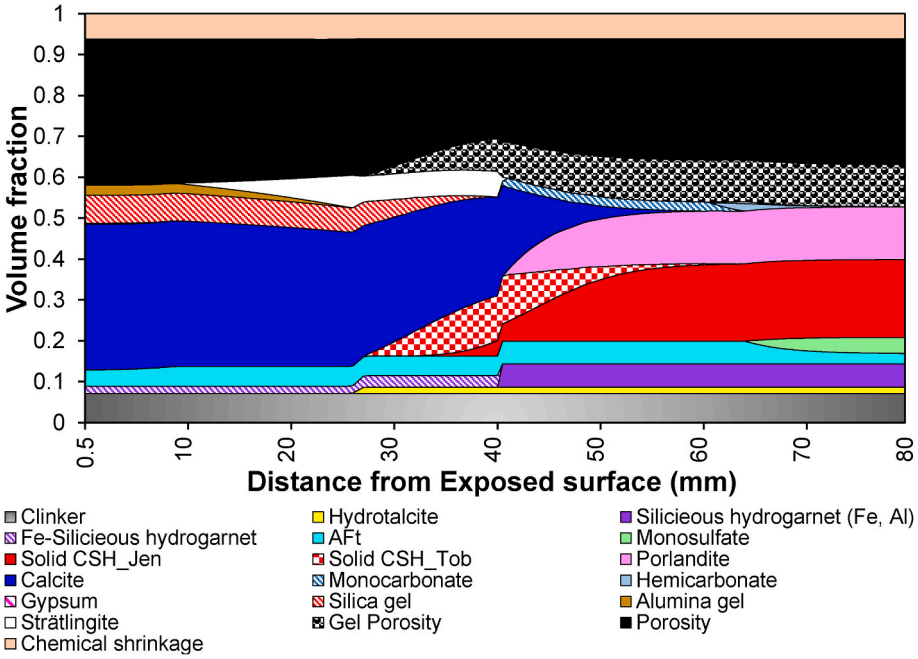

Fig. 5. Phase assemblage of cement paste with W/C of 0.6 exposed in 10 % of CO_2 for 5 years (AFt, solid CSH_Jen and solid CSH_Tob stand for ettringite, solid Jennite type *C*–S–H and solid Tobermorite type *C*–S–H, respectively).

and ettringite. However, the total porosity near to the exposure surface still remains lower compared to the non carbonated matrix. For instance, the total porosity at 80 mm from the exposure surface is approximately 40 %, whereas it is only 32 % at 40 mm from the contact side and around 35 % adjacent to the exposure side.

4.2. Model validation of chloride ion ingression

Model validation with the previously developed model.

Figs. 6 and 7 depict the validation of the proposed transport model with the transport model developed in PHREEQC [28]. The Ordinary Portland cement (clinker composition: C_3S 62.2 %, C_2S 18.3 %, C_3A 5.6 %, C_4AF 9.8 % and Gypsum 3 %, density: 3.16 g/cm^3, Blaine: 311 m^2/kg) with W/C of 0.4 and curing temperature of 20 °C were used as the initial condition for the hydration model. The hydrated matrix was exposed to 500 mol/m^3 of NaCl solution for 30 days after 28 days of hydration (input parameter for transport model). The assumptions considered for this simulation are as follows: i) chloride ion can dissolve in the liquid state of water, ii) the exposure surface is completely submerged, and iii) the total pores system is fully saturated. As shown in Figs. 6 and 7, the predicted results from the proposed model exhibit an excellent agreement with the results from the existing PHREEQC model. However, the ion concentration profile for Ca^{+2} ion shows slight deviation only up to 2.5 mm from the exposed surface, and further increase coincides with the results from the PHREEQC model. The reason could possibly be that the concentration of exposure solution is not constant during the transportation process due to the leaching and diffusion of ions. However, in the proposed model, the specified exposure solution

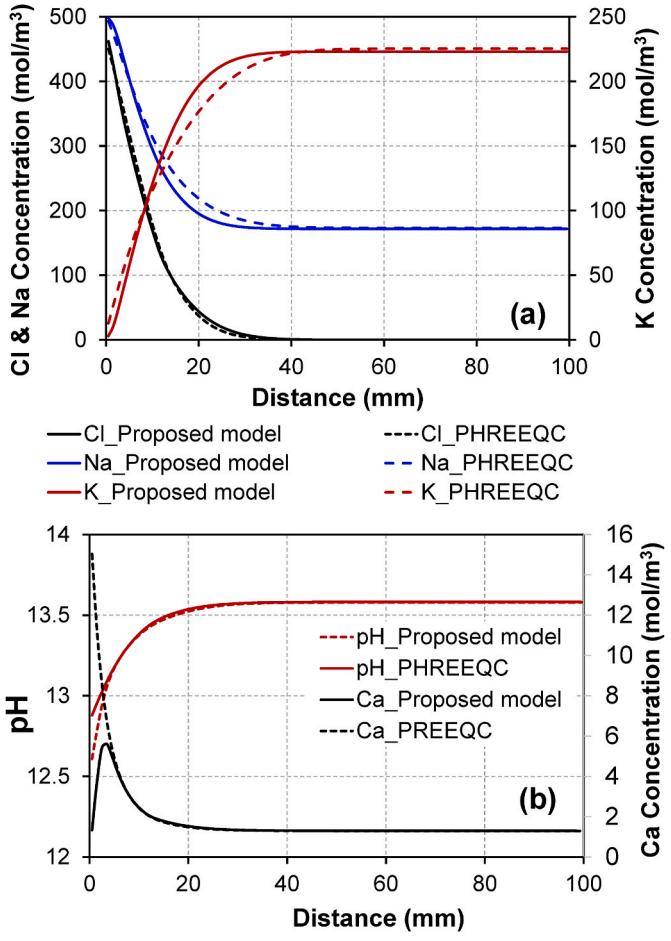

Fig. 6. Ion concentration profiles in the pore solution simulated from the proposed model and PHREEQC model [28].

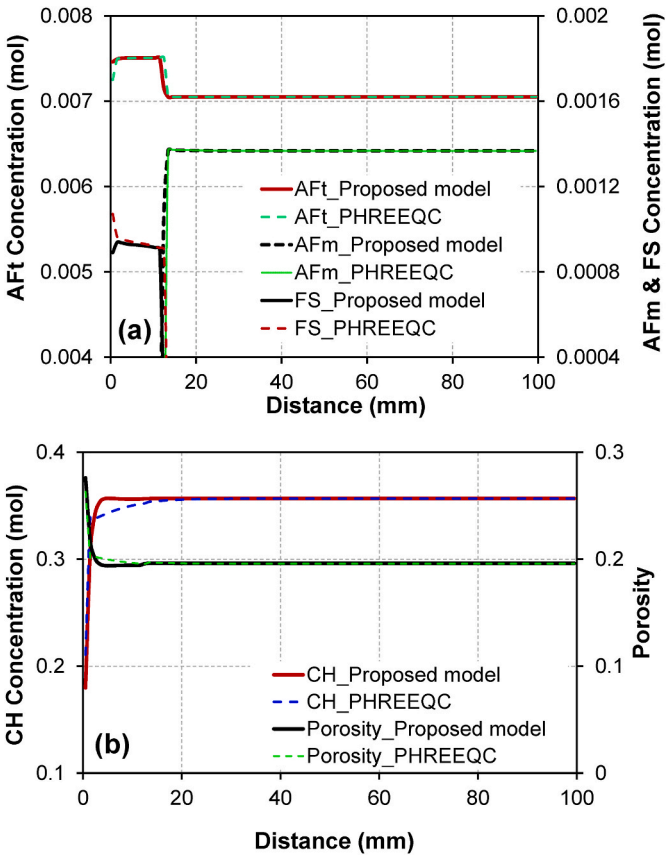

Fig. 7. Comparison of hydrated phases in the hydrated cement paste predicted from the proposed model and PHREEQC model [28] (CH, AFt, AFm and F–S stand for portlandite, ettringite, monosulfate and Friedel's salt, respectively).

by the user is updated for every time step to simulate the actual conditions, like seawater exposure. Therefore, the concentration of leaching ions, including Ca^{+2}, does not accumulate in the exposure solution, while Ca^{+2} concentration accumulates in the previous PHREEQC model.

The concentration of Na^+ and Cl^- are approximately 500 mol/m^3 at the exposed surface due to the high concentration of exposure solution (500 mol/m^3 of NaCl), and then the concentrations of both ions gradually decrease with the distance from the exposed surface as shown in Fig. 6(a). However, after 30 mm from the exposed surface, the Cl^- concentration becomes 0. This could be attributed to the fact that the OPC does not contain Cl^-, and Na^+ concentration is approximately 180 mol/m^3, which is the initial concentration of Na^+ from the 28 days of hydration reaction before the diffusion process. The concentration profile of K^+ shows an increasing tendency with distance up to 30 mm, followed by a constant value of 225 mol/m^3, which is the same as before the transport reaction from the hydration. The K^+ ions are not available in the exposure solution. Therefore, the K^+ leaches from the pore solution to the exposure solution through diffusion due to the concentration gradient between the exposure solution and pore solution (in the hydrated matrix). A similar tendency in the experimental results was also reported by Elakneswaran et al. [28].

Moreover, the pH of the exposure solution and pore solution are about 7.0 and 13.5, respectively. Similar to the leaching of K^+, the OH^- ion also leaches to the exposure solution due to the concentration gradient. Therefore, the pH near the exposed surface is lower than that away from the exposed surface (refer to Fig. 6(b)). Furthermore, the Ca^{+2} concentration profile increases to 5.5 mol/m^3 till 2.5 mm (due to the leaching of Ca^{+2}), decreases to 1.5 mol/m^3 and then unchanged. The peak of the Ca^{+2} profile is due to the dissolution of portlandite (CH), which gives more Ca^{+2} ions in the pore solution, as shown in Figs. 6(b)

and Fig. 7(b). It can be noticed that the portlandite mainly dissolves near the exposed surface due to the leaching of Ca^{+2} in the pore solution and low pH.

The penetrated Cl^- ion is possible to substitute the sulfate ions in AFm-type products like monosulfate ($C_3A.CaSO_4.12H_2O$) to form chloride-containing phases like Friedel's salt ($C_3A.CaCl_2.10H_2O$) as described in Eq. (26). In addition, SO_4^{-2} released from the dissolution of monosulfate to form Friedel's salt (refer Eq. (26)) reacts with existing monosulfate to form the secondary ettringite close to the exposed surface (see Eq. (27)). As a result, Friedel's salt and considerably high amount of ettringite can be found near to the exposed surface, where monosulfate does not appear in the presence of Cl^- ion. As illustrated in Fig. 7(a), the formation of Friedel's salt and a slightly higher amount of ettringite could be seen up to only 15 mm, and afterwards, monosulfate exists. Similar observations were also reported in several previous studies [8,14,15,28].

$$C_3A.CaSO_4.12H_2O + Cl^- \rightarrow C_3A.CaCl_2.10H_2O + SO_4^{-2} \quad (26)$$

$$C_3A.CaSO_4.12H_2O + Ca^{+2} + SO_4^{-2} \rightarrow C_3A.3CaSO_4.32H_2O \quad (27)$$

As depicted in Fig. 7(b), at the exposed surface, the porosity is very higher (approximately 27 %) compared to that away from the exposure surface due to the high dissolution of portlandite up to the point where portlandite dissolves. Afterwards, the porosity remains slightly lower due to the formation of secondary ettringite up to 15 mm, where a high amount of ettringite exists. The porosity value of 19.4 % is in the hydrated matrix away from the degraded area. The amount of *C*–S–H, Fe-siliceous hydrogarnet and hydrotalcite do not show either dissolution or precipitation during the 30 days of transport of ion reactions, revealing constant values as 0.24 mol, 0.023 mol and 0.008 mol for the whole length of specimens, respectively.

4.2.1. Model validation with experimental results

To verify the predictability of the proposed model, the predicted results of the total amount of chloride ion profile are compared with measured values for W/C ranging from 0.3 to 0.5, which have been taken from the study of Mori et al. [58]. The chemical compositions of the clinker used herein are C_3S 65 %, C_2S 11 %, C_3A 9 %, C_4AF 9 % and Gypsum 4 % (density: 3.16 g/cm^3, Blaine: 323 m^2/kg and temperature 20 °C). The cement paste samples (W/C of 0.3, 0.4 and 0.5) were mixed using a mortar mixer, cast in the plastic containers with the dimension of 40 × 60 × 100 mm and sealed. After one day, the specimens were demolded and cured in a moist condition for 28 days. The immersion test was carried out according to JSCE-G572-2003. After taking the samples from the curing tank, five surfaces of rectangular elements were coated with epoxy resin and the samples were exposed to a chloride solution. The exposure condition was 3 % NaCl solution at 20 °C for 91 days. Following the exposure to the NaCl solution, electron probe micro-analysis (EPMA) was used to evaluate the total chloride content in the cement paste. It should be noted that EPMA is the analysis method that allows the quantitative area analysis of elemental concentrations with a high spatial resolution and sensitivity on a solid surface. A specimen of 40 × 40 × 10 mm was sliced as a sample for EPMA measurement. The sliced specimen was strengthened by intrusion with epoxy resin not containing chlorine. The ground specimen for obtaining a smooth surface was dried under a vacuum and coated with carbon for EPMA analysis. Similar to the experimental condition that after the 28 days of hydration samples were kept in 3 % NaCl solution for 91 days, which was used in the proposed model to predict the chloride ion diffusion in the hydrated matrix. As detailed in Fig. 8, the comparison indicates that the predicted results from the developed model exhibit an excellent agreement for w/c of 0.3, 0.4 and 0.5. A slight variation, however, was witnessed near the exposure surface for W/C of 0.3 paste, as shown in Fig. 8(c). For instance, the experimental results for the total chloride weight percentage of W/C 0.3 paste at 1.5 mm from the exposure surface are approximately 1 %, and similar results were obtained for W/C 0.4 paste at the same location. However, due to the lower total porosity of W/C 0.3 paste than 0.4 paste, the total chloride weight percentage should be lower than that of 0.4 W/C paste. Thus, experimental results adjacent to the exposure surface (up to 3.5 mm) of W/C 0.3 paste might be an experimental error.

The penetration of chloride ions in the hydrated matrix increases with W/C, as shown in Fig. 8. Similar behaviour was also reported in the numerous studies for different W/C of concrete and cement paste [22,58,59]. For instance, the penetration depth for W/C 0.3 is approximately 10 mm, while it is about 30 mm for W/C 0.5. Porosity is crucial in studying the effect of W/C on the chloride ion transport for the same exposure conditions and clinker. The porosity directly relates to the

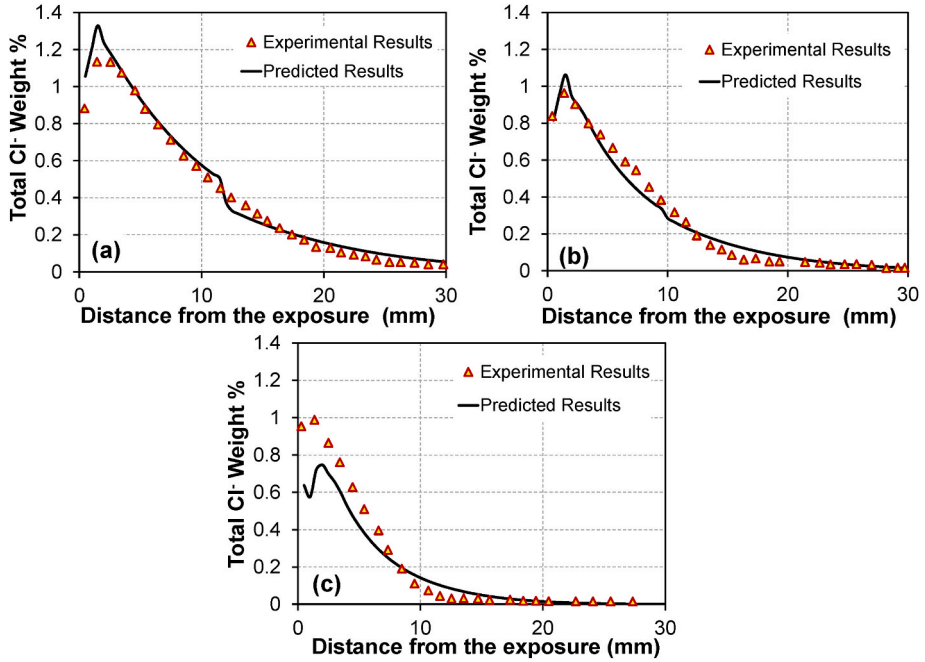

Fig. 8. Numerical and experimental results for chloride ion diffusion for W/C of (a) 0.5, (b) 0.4 and (c) 0.3 [58].

chloride ion's effective diffusion coefficient in the matrix. The porosity of the hydrated matrix increases with W/C owing to the high amount of space employed by water [11,24]. Moreover, due to the 91 days of exposure to NaCl solution, the capillary porosity increases for all the W/C ratio pastes. A similar tendency is also observed in the effective diffusion coefficient with distance from the exposed area, which could be attributed to the changes in capillary porosity.

In this study, two binding mechanisms such as chemical substitution and physical binding, along with the free chloride ion in the pore solution, are herein considered as the types of chloride ion in the hydrated matrix. The numerical results are presented in Fig. 9. The experimental conditions used for Fig. 8 are inputted as initial parameters for this simulation. The simulated results suggest that the above three types of chloride ion concentration profile increase with W/C. The variation of Friedel's salt formed as intruding the chloride ion into the AFm phase and chloride ion adsorption by *C*–S–H surface with distance from the exposed surface for different W/C paste are shown in Fig. 9(a) and (b). The formation of Friedel's salt is considerably higher in 0.5 W/C paste compared to that in 0.4 W/C paste. There is no formation of Friedel's salt in 0.3 paste. Similarly, physical binding by the *C*–S–H surface increases with W/C, as depicted in Fig. 9(b). The above-described tendency for both binding mechanisms is because of the reaction rate of clinker phases and the available chloride ion for the chemical and physical reaction. The well-known fact is that the hydration reaction degree increases with W/C as the available water for the hydration also increases, and it upsurges the reaction of clinker phases, including C_3S, C_2S, C_3A and C_4AF. Thus, the hydration products that bind chlorides, such as *C*–S–H and AFm phases like monosulfate, are highly formed in W/C of 0.5 paste. Moreover, the penetrated chloride also increases with W/C due to the increasing porosity trend. As the combined results, the chemical binding of chloride ion by AFm phases and physically bound chloride by *C*–S–H also increases with W/C. The weight % of chloride ions in the liquid phase is depicted in Fig. 9(c), and as expected, it shows an increasing trend with the W/C ratio. This could be due to high pore volume (porosity) in high W/C paste.

The comparison between experimental and predicted results for the average effective diffusion coefficient of cement paste with W/C ranging from 0.3 to 0.5 exposed in 3 % NaCl solution for 91 days is depicted in Fig. 10. The experimental results were obtained from the study of Mori et al. [58]. The experimental results of the total chloride profiles (see Fig. 8) were used to calculate the average effective diffusion coefficient experimentally by Fick's 2nd law. The concentration of the chloride ion at the surface was reasonably computed by the extrapolation of the profile for the estimation of the effective diffusion coefficient. The average effective diffusion coefficient after 91 days of exposure was then determined by fitting Fick's second law to the concentration profile with the calculated surface concentration. However, this estimation did not consider porosity variation with distance from the exposure surface and chloride binding mechanism (physical and chemical binding) [28,60,61]. The developed model, coupled with thermodynamic calculation, deals with chloride ions' physical and chemical binding. Furthermore, in every meshing point, the thermodynamic and porosity calculations were performed and updated as input parameters into the COMSOL package. Thus, the limitations in Fick's 2nd law were addressed in the proposed model. There is still a slight discrepancy between the predicted and experimental results for the average effective diffusion coefficient of chloride ions, as shown in Fig. 10.

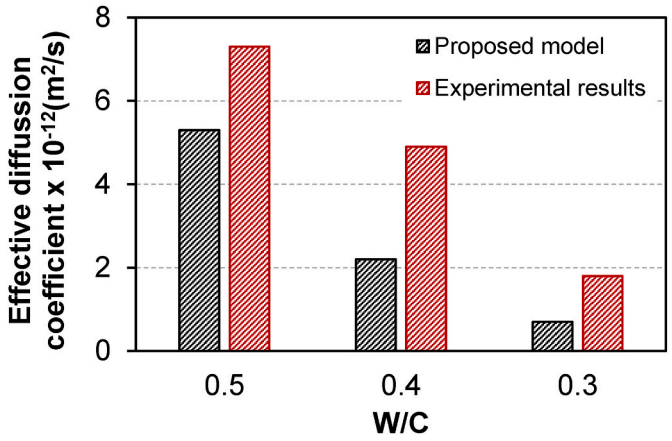

Fig. 10. Comparison of simulated and experimental [58] effective diffusion coefficient for W/C 0.3–0.5 exposed in 3 % NaCl for 91 days.

It is known that the development of *C*–S–H structure and the formation of gel porosity inside the *C*–S–H are more complicated and very hard to simulate to the actual scenario. The gel pores of the *C*–S–H

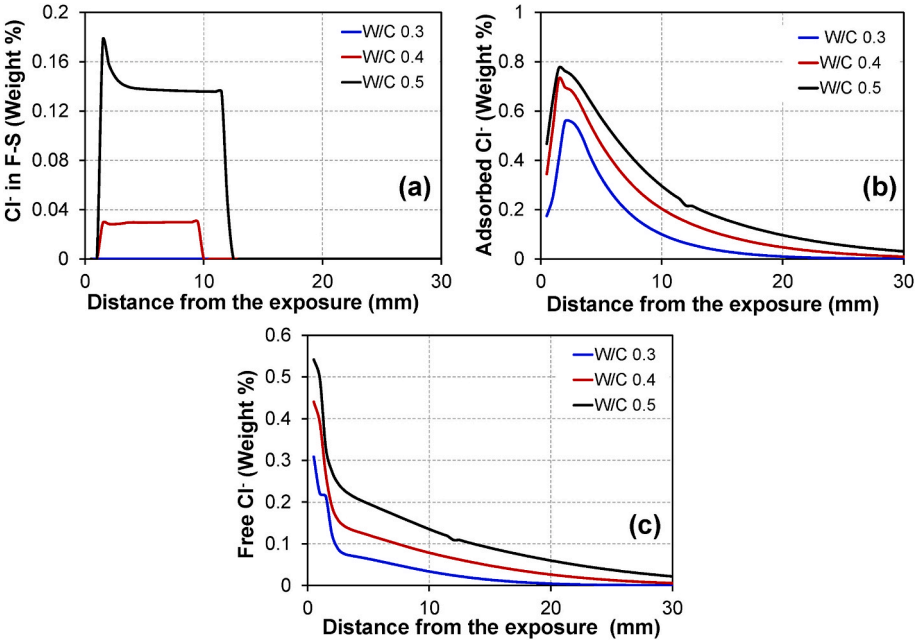

Fig. 9. Variation of (a) chemically bound chloride, (b) physically bound chloride and (c) free chloride with distance from exposure.

progress mainly at an early age (i.e. when the free water in the capillary pores remains significant). After a specific degree of hydration, the gel porosity does not increase due to the transition between the formation of LD and HD *C*–S–H. However, considering the difficulties in simulating the actual condition, throughout the process, the gel porosity of LD *C*–S–H and HD *C*–S–H are considered to be 36 % and 26 %, respectively. These values were adopted from the literature [26]. It should be noted that almost all the previous research works incorporated a constant gel porosity for *C*–S–H matrix, demonstrating the accurate predictions for the hydration, mechanical and transport behaviour of the hydrated cement paste [19,34,37,52].

In this study, the total active porosity for the transportation process is considered as the summation of capillary porosity and gel porosity of LD *C*-SH. Because the porosity accessible by mercury intrusion porosimetry is up to 3 nm in diameter, which includes capillary porosity and a partial amount of gel porosity. Worth noting that the LD *C*–S–H has larger pores than HD *C*–S–H [24,62,63]. The capillary porosity increases with W/C because of the high water content in the matrix. The formation of LD *C*–S–H tends to increase with W/C due to the high available space for precipitation of LD *C*–S–H. Thus, the effective diffusion coefficient of 0.5 paste has a higher value than lower W/C paste, as the total active porosity able to transport the ions and gases increases with the amount of water in the cement mixture (Fig. 10).

4.2.2. *Significance of the proposed model*

The importance of the integrated hydration model with COMSOL Multiphysics for predicting the microstructure of hydrated cement paste during the transportation process is demonstrated in Fig. 11. The cement paste with W/C of 0.35 exposed to 500 mol/m^3 of NaCl solution for 4 years was considered for this simulation. The considered clinker composition consist of C_3S 66.4 %, C_2S 11.8 %, C_3A 8.2 %, C_4AF 9.7 % and gypsum 2.7 %. The phase assemblage of hydrates before the exposure condition is illustrated in Fig. 11(a). Phase assemblage of the hydrated matrix after 4 years of exposure is shown in Fig. 11(b) and **(c).** The volume fraction of the hydrated cement paste shown in Fig. 11(b) is for considering only the transportation process without considering the progression of the hydration reaction during the transportation. Here, the hydration reaction was stopped before initiating the transport reaction. The progression of the hydration and transport reactions is simultaneously considered for numerical results depicted in Fig. 11(c).

Due to the progression of the hydration reaction during the transportation process, the increased amount of hydration products, including *C*–S–H (LD and HD *C*–S–H), portlandite and monosulfate, are observed in the coupled model simulation compared the without considering the progression of hydration reaction. As a result, a reduced amount of capillary porosity can be seen in Fig. 11(c) compared to Fig. 11(b) for the same exposure condition as the formation of products due to the hydration reaction trend to fill the available pore space during the 4 years of the transportation process. Thus, the physically bound chloride by the *C*–S–H and the chemical substitution of chloride ions in monosulfate are considerably high when considering the combined reaction. Owing to the high chloride ion binding capacity by physical and chemical adsorption and low pore space, the free chloride ion, which is a prime factor for initiation of reinforcement corrosion, is significantly low in the actual scenario when considering both hydration and transport reaction simultaneously as presented in Fig. 12. For instance, the predicted concentration of free chloride ion from the case of without progression of hydration model (without hydration) becomes approximately 120 mol/m^3 at 41 mm, whereas a similar concentration is obtained at 26 mm from the coupled reaction model (with hydration). Thus, the depth of chloride ion diffusion is reduced by 15 mm during the 4 years of exposure when considering both hydration and transportation reactions simultaneously.

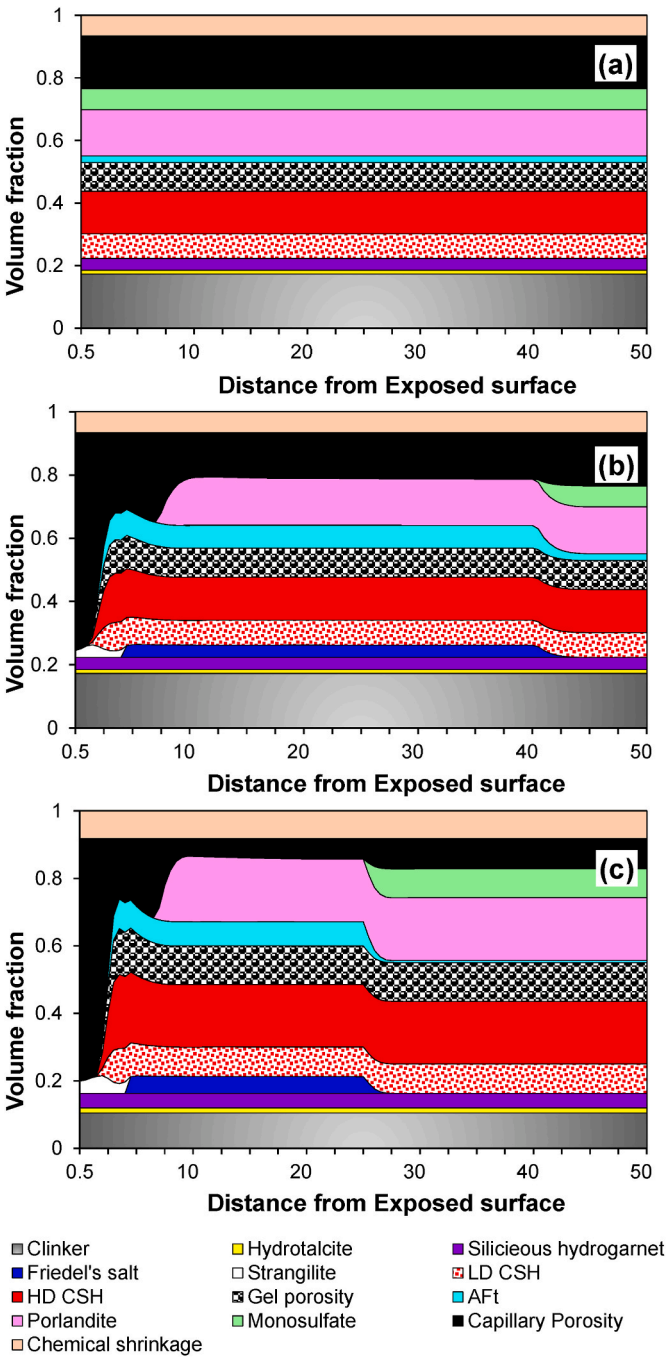

Fig. 11. Distribution of hydrated phases (a) before the exposure condition, (b) after 4 years of exposure without progression of hydration reaction, (c) after 4 years of exposure with the progression of hydration reaction.

5. Conclusions

This paper presented an integrated model describing the diffusion of chloride ions and carbon dioxide gas in the hydrated matrix. The developed model written in MATLAB language coupled with COMSOL Multiphysics considered all the possible mechanisms related to the hydration of cement paste and diffusion of substances in the porous media, including dissolution rate of clinker minerals, chemical reaction during the hydration and transportation process, formation of possible hydrates including two types of *C*–S–H, physical and chemical binding of chloride ion, the dissolution rate of *C*–S–H simultaneously with portlandite during the carbonation and variation of porosity during the hydration

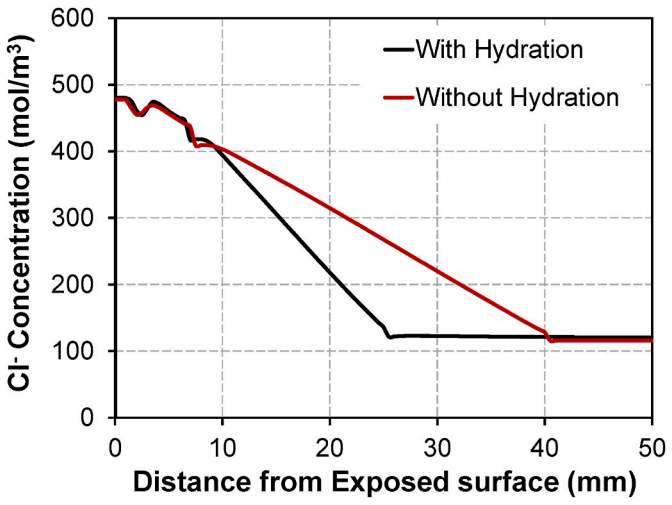

Fig. 12. Comparison of free chloride ion concentration in the pore solution for the cases of with and without progression of hydration reaction.

reaction and transport reaction. The obtained numerical and experimental results lead to the following key conclusions:

In the sight of obtained TGA results for the carbonation of hydrated cement paste, the dissolution rate of portlandite and precipitation of calcite increase with W/C due to high porosity. The predicted results from the coupled model show good agreement with experimental results of the weight percentage of portlandite and calcite for W/C ranging from 0.3 to 0.5 b y considering the simultaneous carbonation of *C*–S–H with portlandite. The proposed transport model developed in MATLAB language coupled with COMSOL Multiphysics for chloride ingression has been validated with previously developed model using the PHREEQC package in terms of ionic concentration in the pore solution and phase assemblage of hydrates. The numerical results of the total chloride profile of cement paste excellently capture the realistic value for W/C ranging from 0.3 to 0.5. The phase assemblage of hydrates in terms of volume fraction of the hydrated cement matrix could be predicted, which comprehensively expresses the variation of phases, including the decalcification of *C*–S–H (from Jennite *C*–S–H to Tobemorite *C*–S–H and finally calcite) during the carbonation with distance from the exposure surface for chloride ion ingression and carbonation. The significance of the simultaneous progression of the hydration reaction with the reaction due to the transport of ions was clearly demonstrated by comparing the results obtained from coupled model (considering the hydration reaction and transport reaction concurrently) with the uncoupled model (only considering the transport reaction) results for phase assemblage of hydrates and free chloride ion profile. The simulation shows that ignoring the hydration reaction of the matrix reveals an increased degradation for chloride ion diffusion.

Declaration of competing interest

The authors declare that they have no known competing financial interests or personal relationships that could have appeared to influence the work reported in this paper.

Data availability

Data will be made available on request.

References

[1] T. Gasch, D. Eriksson, A. Ansell, On the behaviour of concrete at early-ages: a multiphase description of hygro-thermo-chemo-mechanical properties, Cement Concr. Res. 116 (2019) 202–216.
[2] A. Hatanaka, Y. Elakneswaran, K. Kurumisa, T. Nawa, S. Ahmed, K. Azad, K. F. Loughlin, Y. Luan, T. Ishida, T. Sagawa, K. Kurumisawa, The impact of tortuosity on chloride ion diffusion in slag-blended cementitious materials multi-scale modeling of concrete performance-integrated material and structural effect of the key mixture parameters on tortuosity and permeability of concrete enhan, J. Adv. Concr. Technol. 15 (2003) 426–439.
[3] Q.F. Liu, J. Xia, D. Easterbrook, J. Yang, L.Y. Li, Three-phase modelling of electrochemical chloride removal from corroded steel-reinforced concrete, Construct. Build. Mater. 70 (2014) 410–427.
[4] P. Chindaprasirt, S. Rukzon, V. Sirivivatnanon, Effect of carbon dioxide on chloride penetration and chloride ion diffusion coefficient of blended Portland cement mortar, Construct. Build. Mater. 22 (2008) 1701–1707.
[5] M. Xie, P. Dangla, K. Li, Reactive transport modelling of concurrent chloride ingress and carbonation in concrete, Materials and Structures/Materiaux et Constructions, vol. 54, 2021.
[6] X. Shen, Q. Liu, Z. Hu, W. Jiang, X. Lin, D. Hou, P. Hao, Combine ingress of chloride and carbonation in marine-exposed concrete under unsaturated environment: a numerical study, Ocean Eng. 189 (2019), 106350.
[7] S. Sui, W. Wilson, F. Georget, H. Maraghechi, H. Kazemi-Kamyab, W. Sun, K. Scrivener, Quantification methods for chloride binding in Portland cement and limestone systems, Cement Concr. Res. 125 (2019), 105864.
[8] H. Hirao, K. Yamada, H. Takahashi, H. Zibara, Chloride binding of cement estimated by binding isotherms of hydrates, J. Adv. Concr. Technol. 3 (2005) 77–84.
[9] T. Maruya, K. Hsu, H. Takeda, S. Tangtermsirikul, Numerical modeling of steel corrosion in concrete structures due to chloride ion, oxygen and water movement, J. Adv. Concr. Technol. 1 (2003) 147–160.
[10] P.D. Tennis, H.M. Jennings, A model for two types of calcium silicate hydrate in the microstructure of Portland cement pastes, Cement Concr. Res. 30 (2000) 855–863.
[11] S. Krishnya, Y. Yoda, Y. Elakneswaran, A two-stage model for the prediction of mechanical properties of cement paste, Cem. Concr. Compos. 115 (2021), 103853.
[12] M.R. Jones, D.E. Macphee, J.A. Chudek, G. Hunter, R. Lannegrand, R. Talero, S. N. Scrimgeour, Studies using 27Al MAS NMR of AFm and AFt phases and the formation of Friedel's salt, Cement Concr. Res. 33 (2003) 177–182.
[13] Y. Elakneswaran, T. Nawa, K. Kurumisawa, Electrokinetic potential of hydrated cement in relation to adsorption of chlorides, Cement Concr. Res. 39 (2009) 340–344.
[14] M.V.A. Florea, H.J.H. Brouwers, Chloride binding related to hydration products: Part I: ordinary Portland Cement, Cement Concr. Res. 42 (2012) 282–290.
[15] B. Guo, Y. Hong, G. Qiao, J. Ou, A COMSOL-PHREEQC interface for modeling the multi-species transport of saturated cement-based materials, Construct. Build. Mater. 187 (2018) 839–853.
[16] X. You, X. Hu, P. He, J. Liu, C. Shi, A review on the modelling of carbonation of hardened and fresh cement-based materials, Cem. Concr. Compos. 125 (2022), 104315.
[17] B. Šavija, M. Luković, Carbonation of cement paste: understanding, challenges, and opportunities, Construct. Build. Mater. 117 (2016) 285–301.
[18] S. von Greve-Dierfeld, B. Lothenbach, A. Vollpracht, B. Wu, B. Huet, C. Andrade, C. Medina, C. Thiel, E. Gruyaert, H. Vanoutrive, I.F. Saéz del Bosque, I. Ignjatovic, J. Elsen, J.L. Provis, K. Scrivener, K.C. Thienel, K. Sideris, M. Zajac, N. Alderete, Ö. Cizer, P. Van den Heede, R.D. Hooton, S. Kamali-Bernard, S.A. Bernal, Z. Zhao, Z. Shi, N. De Belie, Understanding the Carbonation of Concrete with Supplementary Cementitious Materials: a Critical Review by RILEM TC 281-CCC, 2020.
[19] Q.T. Phung, N. Maes, D. Jacques, G. De Schutter, G. Ye, J. Perko, Modelling the carbonation of cement pastes under a CO2 pressure gradient considering both diffusive and convective transport, Construct. Build. Mater. 114 (2016) 333–351.
[20] B. Song, C. Shi, X. Hu, K. Ouyang, Y. Ding, G. Ke, Effect of early CO2 curing on the chloride transport and binding behaviors of fly ash-blended Portland cement, Construct. Build. Mater. 288 (2021), 123113.
[21] P.H.R. Borges, J.O. Costa, N.B. Milestone, C.J. Lynsdale, R.E. Streatfield, Carbonation of CH and C–S–H in composite cement pastes containing high amounts of BFS, Cement Concr. Res. 40 (2010) 284–292.
[22] Y. Hosokawa, K. Yamada, H. Takahashi, Time dependency of Cl diffusion coefficients in concretes with varied phase compositions and pore structures under different environmental conditions, J. Adv. Concr. Technol. 10 (2012) 363–374.
[23] R.A. Patel, Q.T. Phung, S.C. Seetharam, J. Perko, D. Jacques, N. Maes, G. de Schutter, G. Ye, K. van Breugel, Diffusivity of saturated ordinary Portland cement-based materials: a critical review of experimental and analytical modelling approaches, Cement Concr. Res. 90 (2016) 52–72.
[24] C. Li, S. Krishnya, M. Ogino, E. Owaki, Y. Elakneswaran, Investigating the hydration characteristics of a new composite cementitious binder containing of slag and calcite, Construct. Build. Mater. 361 (2022), 129629.
[25] M. Hlobil, V. Šmilauer, G. Chanvillard, Micromechanical multiscale fracture model for compressive strength of blended cement pastes, Cement Concr. Res. 83 (2016) 188–202.
[26] H.M. Jennings, J.J. Thomas, J.S. Gevrenov, G. Constantinides, F.J. Ulm, A multi-technique investigation of the nanoporosity of cement paste, Cement Concr. Res. 37 (2007) 329–336, https://doi.org/10.1016/j.cemconres.2006.03.021.
[27] V.J. Azad, C. Li, C. Verba, J.H. Ideker, O.B. Isgor, A COMSOL-GEMS interface for modeling coupled reactive-transport geochemical processes, Comput. Geosci. 92 (2016) 79–89.
[28] Y. Elakneswaran, A. Iwasa, T. Nawa, T. Sato, K. Kurumisawa, Ion-cement hydrate interactions govern multi-ionic transport model for cementitious materials, Cement Concr. Res. 40 (2010) 1756–1765.

[29] O. Omikrine Metalssi, A. Aït-Mokhtar, P. Turcry, A proposed modelling of coupling carbonation-porosity-moisture transfer in concrete based on mass balance equilibrium, Construct. Build. Mater. 230 (2020), 116997.
[30] B. Bary, A. Sellier, Coupled moisture - carbon dioxide-calcium transfer model for carbonation of concrete, Cement Concr. Res. 34 (2004) 1859–1872.
[31] D.P. Bentz, Influence of water-to-cement ratio on hydration kinetics: simple models based on spatial considerations, Cement Concr. Res. 36 (2006) 238–244.
[32] X.Y. Wang, H.S. Lee, Modeling the hydration of concrete incorporating fly ash or slag, Cement Concr. Res. 40 (2010) 984–996.
[33] L.J. Parrot, D.C. Killoh, Prediction of cement hydration, Br. Ceram. Proc. 35 (1984) 41–53.
[34] B. Lothenbach, T. Matschei, G. Möschner, F.P. Glasser, Thermodynamic modelling of the effect of temperature on the hydration and porosity of Portland cement, Cement Concr. Res. 38 (2008) 1–18.
[35] B. Lothenbach, F. Winnefeld, Thermodynamic modelling of the hydration of Portland cement, Cement Concr. Res. 36 (2006) 209–226.
[36] S. Krishnya, Y. Elakneswaran, Y. Yoda, Proposing a three-phase model for predicting the mechanical properties of mortar and concrete, Mater. Today Commun. 29 (2021), 102858.
[37] J. Zheng, X. Zhou, X. Jin, An n-layered spherical inclusion model for predicting the elastic moduli of concrete with inhomogeneous ITZ, Cem. Concr. Compos. 34 (2012) 716–723.
[38] Y. Elakneswaran, E. Owaki, S. Miyahara, M. Ogino, T. Maruya, T. Nawa, Hydration study of slag-blended cement based on thermodynamic considerations, Construct. Build. Mater. 124 (2016) 615–625.
[39] D.L. Parkhurst, C.A.J. Appelo, A Computer Program for Speciation, Batch-Reaction, One-Dimensional Transport and Inverse Geochemical Calculations, USGS Report, 1999.
[40] T. Sanchez, P. Henocq, O. Millet, A. Aït-Mokhtar, Coupling PhreeqC with Electro-Diffusion Tests for an Accurate Determination of the Diffusion Properties on Cementitious Materials, 2019.
[41] N. Holmes, M. Tyrer, R. West, A. Lowe, D. Kelliher, Using PHREEQC to model cement hydration, Construct. Build. Mater. 319 (2022).
[42] B. Lothenbach, D.A. Kulik, T. Matschei, M. Balonis, L. Baquerizo, B. Dilnesa, G. D. Miron, R.J. Myers, Cemdata18: a chemical thermodynamic database for hydrated Portland cements and alkali-activated materials, Cement Concr. Res. 115 (2019) 472–506.
[43] B. Lothenbach, Thermodynamic equilibrium calculations in cementitious systems, Mater. Structures/Materiaux et Construct. 43 (2010) 1413–1433.
[44] V.Q. Tran, A. Soive, V. Baroghel-Bouny, Modelisation of chloride reactive transport in concrete including thermodynamic equilibrium, kinetic control and surface complexation, Cement Concr. Res. 110 (2018) 70–85.
[45] M. Balonis, B. Lothenbach, G. le Saout, F.P. Glasser, Impact of chloride on the mineralogy of hydrated Portland cement systems, Cement Concr. Res. 40 (2010) 1009–1022.
[46] Y. Suda, T. Saeki, T. Saito, Y. Aono, F. Matsushita, S. Shibata, Y. Hama, T. Saeki, Relation between chemical composition and physical properties of C-S-H generated from cementitious materials nano-structural changes of C-S-H in hardened cement paste during drying at 50°C relation between chemical composition and physical properties of C-S-H generated from cementitious materials, Go Igarashi J. Adv. Concrete Technol. 13 (2015) 275–290.
[47] A. Nonat, H. Ene Viallis-Terrisse, J.-C. Petit, Zeta-potential study of calcium silicate hydrates interacting with alkaline cations, J. Colloid Interface Sci. 244 (2001) 58–65.
[48] D.A. Kulik, M. Kersten, Aqueous solubility diagrams for cementitious waste stabilization systems: II, end-member stoichiometries of ideal calcium silicate hydrate solid solutions, J. Am. Ceram. Soc. 84 (2001) 3017–3026.
[49] Z. Shi, B. Lothenbach, M.R. Geiker, J. Kaufmann, A. Leemann, S. Ferreiro, J. Skibsted, Experimental studies and thermodynamic modeling of the carbonation of Portland cement, metakaolin and limestone mortars, Cement Concr. Res. 88 (2016) 60–72.
[50] A. Morandeau, M. Thiéry, P. Dangla, Impact of accelerated carbonation on OPC cement paste blended with fly ash, Cement Concr. Res. 67 (2015) 226–236.
[51] A. Morandeau, M. Thiéry, P. Dangla, Investigation of the carbonation mechanism of CH and C-S-H in terms of kinetics, microstructure changes and moisture properties, Cement Concr. Res. 56 (2014) 153–170.
[52] T. Ishida, C.-H. Li, Modeling of carbonation based on thermo-hygro physics with strong coupling of mass transport and equilibrium in micro-pore structure of concrete, J. Adv. Concr. Technol. 6 (2008) 303–316.
[53] B.Y.D.P. Bentz, P. Lura, J.W. Roberts, Mixture proportioning for internal curing, Concr. Int. (2005) 35–40.
[54] O.O. Metalssi, A. Aït-Mokhtar, P. Turcry, A Proposed Modelling of Coupling Carbonation-Porosity-Moisture Transfer in Concrete Based on Mass Balance Equilibrium, 2019.
[55] T. Ishida, P.O.N. Iqbal, H.T.L. Anh, Modeling of chloride diffusivity coupled with non-linear binding capacity in sound and cracked concrete, Cement Concr. Res. 39 (2009) 913–923.
[56] V. Shah, K. Scrivener, B. Bhattacharjee, S. Bishnoi, Changes in microstructure characteristics of cement paste on carbonation, Cement Concr. Res. 109 (2018) 184–197.
[57] F. Deschner, F. Winnefeld, B. Lothenbach, S. Seufert, P. Schwesig, S. Dittrich, F. Goetz-Neunhoeffer, J. Neubauer, Hydration of Portland cement with high replacement by siliceous fly ash, Cement Concr. Res. 42 (2012) 1389–1400.
[58] D. Mori, K. Yamada, Y. Hosokawa, M. Yamamoto, Applications of electron probe microanalyser for measurement of Cl concentration profile in concrete, J. Adv. Concr. Technol. 4 (2006) 369–383.
[59] S.H. Han, Influence of diffusion coefficient on chloride ion penetration of concrete structure, Construct. Build. Mater. 21 (2007) 370–378.
[60] X. Du, L. Jin, R. Zhang, Chloride Diffusivity in Saturated Cement Paste Subjected to External Mechanical Loadings, 2014.
[61] Z. Song, L. Jiang, H. Chu, C. Xiong, R. Liu, L. You, Modeling of chloride diffusion in concrete immersed in CaCl2 and NaCl solutions with account of multi-phase reactions and ionic interactions, Construct. Build. Mater. 66 (2014) 1–9.
[62] N. Noguchi, S. Krishnya, T. Chabayashi, H. Kato, T. Nawa, Y. Elakneswaran, Hydration of ferrite-rich Portland cement: evaluation of Fe-hydrates and Fe uptake in calcium-silicate-hydrates, Construct. Build. Mater. 288 (2021), 123142.
[63] S. Krishnya, C. Herath, Y. Elakneswaran, C. Gunasekara, D.W. Law, S. Setunge, Modeling of hydration products and strength development for high-volume fly ash binders, Construct. Build. Mater. 320 (2022), 126228.